# NASA Technical Memorandum 102731

NASA-TM-102731 19910002361

# THREE-DIMENSIONAL FLUX-SPLIT EULER SCHEMES INVOLVING UNSTRUCTURED DYNAMIC MESHES

JOHN T. BATINA



NOVEMBER 1990

National Aeronautics and
Space Administration

**Langley Research Center**
Hampton, Virginia 23665

# THREE-DIMENSIONAL FLUX-SPLIT EULER SCHEMES INVOLVING UNSTRUCTURED DYNAMIC MESHES

John T. Batina*
NASA Langley Research Center
Hampton, Virginia 23665-5225

## Abstract

Improved algorithms for the solution of the three-dimensional time-dependent Euler equations are presented for aerodynamic analysis involving unstructured dynamic meshes. The improvements have been developed recently to the spatial and temporal discretizations used by unstructured grid flow solvers. The spatial discretization involves a flux-split approach which is naturally dissipative and captures shock waves sharply with at most one grid point within the shock structure. The temporal discretization involves either an explicit time-integration scheme using a multi-stage Runge-Kutta procedure or an implicit time-integration scheme using a Gauss-Seidel relaxation procedure which is computationally efficient for either steady or unsteady flow problems. With the implicit Gauss-Seidel procedure, very large time steps may be used for rapid convergence to steady state, and the step size for unsteady cases may be selected for temporal accuracy rather than for numerical stability. Steady flow results are presented for both the NACA 0012 airfoil and the ONERA M6 wing to demonstrate applications of the new Euler solvers. The paper presents a description of the Euler solvers along with results and comparisons which assess the capability.

## Introduction

Considerable progress has been made over the past two decades on developing computational fluid dynamics (CFD) methods for aerodynamic analysis.[1,2] Recent work in CFD has focused primarily on developing algorithms for the solution of the Euler and Navier-Stokes equations. These methods of solution typically assume that the computational grid has an underlying geometrical structure. As an alternative, algorithms have been developed recently which make use of unstructured grids.[3-16] In two dimensions these grids are typically made up of triangles and in three dimensions they consist of an assemblage of tetrahedra. The unstructured grid methods have been demonstrated to have distinct advantages over structured grid methods in that they can easily treat the most complex of geometric configurations and they also easily allow for adaptive mesh refinement to treat very complicated flow physics. Both of these advantages result from the flexibility of orienting and numbering the elements which make up the mesh in an arbitrary fashion. Many of the methods based on unstructured grids, however, use a spatial discretization based on central differencing with explicit artificial dissipation, and use temporal discretizations involving explicit time-marching such as a multi-stage Runge-Kutta time integration. The explicit artificial dissipation used in such schemes tends to smear shock waves over several grid cells and requires the tuning of free parameters that scale the dissipation. Also, the explicit time-integration has a step size that is limited by the Courant-Friedricks-Lewy (CFL) condition to very small values. Consequently, thousands (and occasionally tens of thousands) of time steps are required to obtain steady-state solutions, and thousands of steps per cycle of motion are required for unsteady solutions. Therefore, the purpose of the paper is to report on improvements that have been developed recently to the spatial and temporal discretizations of the unstructured grid flow solvers which resolve the numerical issues described above. The spatial discretization now involves a so-called flux-split approach based on the flux-vector splitting of van Leer.[17] The flux-split discretization accounts for the local wave-propagation characteristics of the flow and captures shock waves sharply with at most one grid point within the shock structure. A further advantage is that the discretization is naturally dissipative and consequently does not require additional artificial dissipation terms or the adjustment of free parameters to control the dissipation. Furthermore, in addition to an explicit time-integration scheme involving a multi-stage Runge-Kutta procedure, the temporal discretization can alternatively be based on an implicit time-integration scheme involving a Gauss-Seidel relaxation procedure. This relaxation procedure is stable for very large time steps and thus allows the selection of the step size based on the temporal accuracy dictated by the problem being considered, rather than on the numerical stability of the algorithm. Consequently, very large time steps may be used for rapid convergence to steady state, and an appropriate step size may be selected for unsteady cases, independent of numerical stability issues. The work reported herein represents the extension to three dimensions of some of the methods developed originally by the author in two dimensions.[18] In Ref. 18, steady and unsteady flow results demonstrated the accuracy and efficiency of the improvements to the spatial and temporal discretizations for the NACA 0012 airfoil. To assess the performance of the three-dimensional algorithm, calculations were performed for the ONERA M6 wing[19] at a freestream Mach number of $M_\infty = 0.84$ and an angle of attack of $\alpha = 3.06°$. This case is an AGARD standard case for the assessment of inviscid flowfield methods,[19] where experimental steady pressure data are available for comparison with calculated pressures.

## Euler Equations

In the present study the flow is assumed to be governed by the three-dimensional time-dependent Euler equations which may be written in integral form as

$$\frac{\partial}{\partial t}\int_\Omega Q\,dV + \int_{\partial\Omega}(En_x + Fn_y + Gn_z)\,dA = 0 \qquad (1)$$

where Q is the vector of conserved variables representing mass, momenta, and energy, and E, F, and G are the convective fluxes in the x, y, and z directions, respectively. The second term is a boundary integral resulting from application of the divergence theorem.

## Spatial Discretization

The spatial discretization is based on Van Leer's[17] flux-vector splitting which is herein implemented as a cell-centered scheme where the flow variables are stored at the centroid of each tetrahedra and the control volume is simply the tetrahedra itself. Consequently the spatial discretization involves a flux balance where the fluxes along the four faces of a given tetrahedra are summed as

$$\sum H A_s = \sum T(EA_x + FA_y + GA_z) \qquad (2)$$

*Senior Research Scientist, Unsteady Aerodynamics Branch, Structural Dynamics Division, Senior Member AIAA

N91-11674#

where T is a transformation matrix which is required to rotate the fluxes into a locally Cartesian coordinate system that has a coordinate direction normal to the face. In Eq. (2) $A_x$, $A_y$, and $A_z$ are the directed areas of the face in the x, y, and z coordinate directions, respectively, and $A_s^2 = A_x^2 + A_y^2 + A_z^2$. In general, the flux vector H is split in a one-dimensional fashion into forward (H+) and backward (H-) vectors as

$$H = H^+(q^-) + H^-(q^+) \tag{3}$$

where the notation $H^+(q^-)$ and $H^-(q^+)$ indicates that the fluxes $H^\pm$ are evaluated using upwind-biased interpolations of the primitive variables q. In two-dimensions for a given triangle j, for example, and considering the diagram in Fig. 1(a), the upwind-biased interpolation for $q^-$ along the edge between triangles j and k is defined by

$$q^- = q_j + \frac{1}{4}[(1-\kappa)\Delta_- + (1+\kappa)\Delta_+] \tag{4}$$

where
$$\Delta_+ = q_k - q_j \tag{5a}$$
$$\Delta_- = q_j - q_i \tag{5b}$$

In Eqs. (4) and (5), $q_j$ and $q_k$ are the vectors of primitive variables at the centroids of triangles j and k, respectively, and $q_i$, the vector of primitive variables at node i, is determined by an average of the flow variables in the triangles surrounding node i. The upwind-biased interpolation for $q^+$ along this edge is determined similarly using the flow variables at centroids j and k and the flow variables at node l. In three-dimensions a similar interpolation procedure is used where $q_j$ and $q_k$ are the vectors of primitive variables at the centroids of tetrahedra j and k, respectively, and $q_i$, the vector of primitive variables at node i, is determined by an average of the flow variables in the tetrahedra surrounding node i.

The parameter $\kappa$ in Eq. (4) controls a family of difference schemes by appropriately weighting $\Delta_-$ and $\Delta_+$. On structured meshes it is easy to show that $\kappa = -1$ yields a fully upwind scheme, $\kappa = 0$ yields Fromm's scheme, and $\kappa = 1$ yields central differencing. The value $\kappa = 1/3$ leads to a third-order-accurate upwind-biased scheme, although third-order accuracy is strictly correct only for one-dimensional calculations. Nevertheless, $\kappa = 1/3$ was used in the calculations presented herein.

On highly stretched meshes in two dimensions, the formula for $\Delta_+$ is modified to be

$$\Delta_+ = \frac{2a}{a+b}(q_k - q_j) \tag{6}$$

where a and b are the distances from the midpoint of the edge to the centroids of triangles j and k, respectively, as shown in Fig. 1(b). This formula weights the flow variables in the interpolation formula (Eq. (4)) differently to account for the stretching of the mesh. For example, by substituting Eq. (6) into Eq. (4) and letting $\kappa = 1$ yields

$$q^- = \frac{b}{a+b}q_j + \frac{a}{a+b}q_k \tag{7}$$

For the case shown in Fig. 1(b), Eq. (7) clearly gives more weight in the calculation of $q^-$ to the flow variables at centroid j than to the flow variables at centroid k, since b>a. On highly stretched meshes in three dimensions, a modified formula similar to Eq. (6) is also used. Futhermore, in calculations involving upwind-biased schemes, oscillations in the solution near shock waves are expected to occur. To eliminate these oscillations flux limiting is usually required. The flux limiter modifies the upwind-biased interpolations for $q^-$ and $q^+$ such that, for example

$$q^- = q_j + \frac{s}{4}[(1-\kappa s)\Delta_- + (1+\kappa s)\Delta_+] \tag{8}$$

where s is the flux limiter. In the present study, a continuously differentiable flux limiter was employed which is defined by

$$s = \frac{2\Delta_-\Delta_+ + \varepsilon}{\Delta_-^2 + \Delta_+^2 + \varepsilon} \tag{9}$$

where $\varepsilon$ is a very small number to prevent division by zero in smooth regions of the flow.

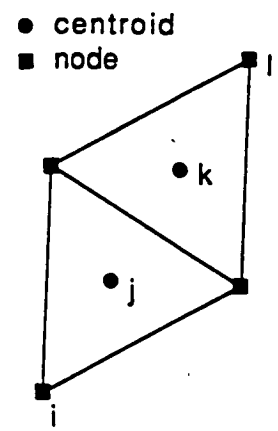


(a) centroids and nodes used in construction of upwind-biased flow variables.

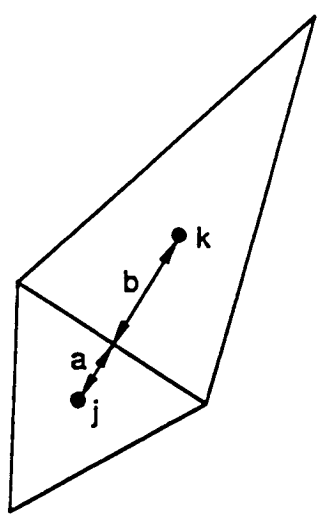


(b) distances between centroids and midpoint of edge used in Eqs. (6) and (7).

Fig. 1 Diagrams illustrating details of the flux-split Euler algorithm implementation.

## Temporal Discretization

The unsteady Euler equations may be integrated in time using either explicit or implicit time-marching procedures. Each of these procedures is described briefly in the following subsections.

### Explicit Time-Marching

The Euler equations are integrated in time by assuming that the conserved variables represented by Q are constant within a control volume which yields

$$\frac{d}{dt}(V\,Q) + C(Q) = 0 \qquad (10)$$

where C represents the convective fluxes and V is the volume of a given tetrahedron. These equations are integrated in time using an explicit four-stage Runge-Kutta time-stepping scheme given by

$$\begin{aligned} Q^{(0)} &= Q^n \\ Q^{(1)} &= Q^{(0)} - \tfrac{1}{4}\frac{\Delta t}{V} C(Q^{(0)}) \\ Q^{(2)} &= Q^{(0)} - \tfrac{1}{3}\frac{\Delta t}{V} C(Q^{(1)}) \\ Q^{(3)} &= Q^{(0)} - \tfrac{1}{2}\frac{\Delta t}{V} C(Q^{(2)}) \\ Q^{(4)} &= Q^{(0)} - \frac{\Delta t}{V} C(Q^{(3)}) \\ Q^{n+1} &= Q^{(4)} \end{aligned} \qquad (11)$$

To accelerate convergence to steady state, implicit residual smoothing and local time-stepping are used. The residual smoothing allows the use of CFL numbers that are larger than that dictated by the stability of the original scheme. This is accomplished by averaging implicitly the residual with values at neighboring grid points. These implicit equations are solved approximately by using several Jacobi iterations. The local time-stepping uses a maximum allowable step size at each grid point as determined by a local stability analysis.

### Implicit Time-Marching

The implicit algorithm is formulated by first approximating the time derivative in the Euler equations by

$$\frac{\partial Q}{\partial t} = \frac{2+\phi}{2}\frac{\Delta Q}{\Delta t} + \frac{2+\phi}{2}\frac{Q^* - Q^n}{\Delta t} - \frac{\phi}{2}\frac{Q^n - Q^{n-1}}{\Delta t} \qquad (12)$$

where $\Delta Q = Q^{n+1} - Q^*$ and where the parameter $\phi$ controls the temporal order of accuracy. For example, the scheme is first-order-accurate in time if $\phi = 0$ and the scheme is second-order-accurate in time if $\phi = 1$. For an implicit temporal discretization, the flux H must be treated at time level (n+1) which is accomplished by linearizing according to

$$H^{n+1} = H^* + \frac{\partial H}{\partial Q}\Big|_{Q=Q^*} \Delta Q \qquad (13)$$

where $\partial H/\partial Q$ is the flux jacobian A. Also, Eqs. (12) and (13) involve $Q^*$, the vector of flow variables at an iterate level (*) which is normally taken to be time level (n). For unsteady applications, however, subiterations may be performed to drive $Q^*$ to $Q^{n+1}$ and thus minimize linearization and relaxation errors.

With the flux-split spatial discretization, the forward and backward fluxes are linearized for a given tetrahedron j as

$$\sum T^{-1}[H^+(q^-)+H^-(q^+)]^{n+1}A_s = \sum T^{-1}[H^+(q^-)+H^-(q^+)]^* A_s + [\sum T^{-1}A^+A_s]\Delta Q_j + \sum_{m=1}^{4} T^{-1}A^-A_s\Delta Q_m \qquad (14)$$

In this equation the last summation on the right hand side involves $\Delta Q_m$, the change in the flow variables in the four tetrahedra adjacent to tetrahedron j. Also, the exact jacobians $A^+$ and $A^-$ are determined by differentiation of $H^+$ and $H^-$ by the conserved variables Q. By combining Eqs. (12) and (14), the Euler equations are discretized as

$$\left[\frac{2+\phi}{2}\frac{V}{\Delta t} I + \sum T^{-1}A^+ A_s\right]\Delta Q_j + \sum_{m=1}^{4} T^{-1}A^- A_s\,\Delta Q_m = -\frac{2+\phi}{2}\frac{Q^* - Q^n}{\Delta t}V + \frac{\phi}{2}\frac{Q^n - Q^{n-1}}{\Delta t}V - \sum T^{-1}[H^+(q^-)+H^-(q^+)]^* A_s \qquad (15)$$

where I is the identity matrix. Direct solution of the system of simultaneous equations which results from application of Eq. (15) for all tetrahedra in the mesh, requires the inversion of a large matrix with large bandwidth which is computationally expensive. Instead, a Gauss-Seidel relaxation approach is used to solve the equations whereby the summation involving $\Delta Q_m$ is moved to the right hand side of Eq. (15). The terms in this summation are then evaluated for a given time step using the most recently computed values for the $\Delta Q$'s. The solution procedure then involves only the inversion of a 5 x 5 matrix (represented by the terms in square brackets on the left hand side of Eq. (15)) for each tetrahedra in the mesh. The procedure is implemented by first ordering the elements that make up the unstructured mesh from upstream to downstream, and the solution is obtained by sweeping two times through the mesh as dictated by stability considerations. The first sweep is performed in the direction from upstream to downstream and the second sweep is from downstream to upstream. For purely supersonic flows the second sweep is unnecessary.

## Boundary Conditions

To impose the flow tangency boundary condition along the surface of the vehicle, the flow variables are set within dummy cells that are effectively inside the geometry being considered. The velocity components within a dummy cell, $(u, v, w)_d$, are determined from the values in the cell j adjacent to the surface, $(u, v, w)_j$. This is accomplished by first rotating the components into a coordinate system that has a coordinate direction normal to the boundary face. The sign of the velocity component in this direction is changed (hence imposing no flow through the face) and the three velocity components are then rotated back into the original x, y, z coordinate system. After considerable algebra this yields

$$\begin{Bmatrix} u \\ v \\ w \end{Bmatrix}_d = \begin{bmatrix} 1-2n_x^2 & -2n_x n_y & -2n_x n_z \\ -2n_x n_y & 1-2n_y^2 & -2n_y n_z \\ -2n_x n_z & -2n_y n_z & 1-2n_z^2 \end{bmatrix} \begin{Bmatrix} u \\ v \\ w \end{Bmatrix}_j \qquad (16)$$

where $n_x$, $n_y$, and $n_z$ are the x, y, and z components of the unit vector that is normal to the boundary face. Also, pressure and density within the dummy cell are set equal to the values in the cell adjacent to the surface.

After application of the upwind-biased interpolation formula to determine $q^-$ and $q^+$ at each face, the velocity components are corrected to give a "strong" implementation of the surface boundary condition according to

$$u_{corrected} = u - n_x (un_x + vn_y + wn_z)$$
$$v_{corrected} = v - n_y (un_x + vn_y + wn_z) \qquad (17)$$
$$w_{corrected} = w - n_z (un_x + vn_y + wn_z)$$

In the far field a characteristic analysis based on Riemann invariants is used to determine the values of the flow variables on the outer boundary of the grid. This analysis correctly accounts for wave propagation in the far field which is important for rapid convergence to steady-state and serves as a "nonreflecting" boundary condition for unsteady applications.

## Results and Discussion

To assess the accuracy and efficiency of the unstructured-grid upwind-Euler algorithm and to demonstrate several of the basic features of the scheme, calculations were first performed in two dimensions for the NACA 0012 airfoil. These results were obtained using the unstructured grid shown in Fig. 2. The grid has 3300 nodes, 6466 triangles, and extends 20 chordlengths from the airfoil with a circular outer boundary. Also there are 110 points that lie on the airfoil surface. Steady-state calculations were performed for the airfoil at a freestream Mach number of $M_\infty = 0.8$ and an angle of attack of $\alpha = 1.25°$. The results were obtained using both the implicit relaxation time-marching scheme and the explicit four-stage Runge-Kutta time-marching scheme. The explicit time-marching results were obtained using a CFL number of 2.5 (since the CFL limit is approximately 2.8) and the implicit time-marching results were obtained using a CFL number of 100,000. Such a large value was used for the implicit results since the relaxation scheme has maximum damping and hence fastest convergence for very large time steps. This is in contrast with implicit approximate factorization schemes which have maximum damping for CFL numbers on the order of 10.

A comparison of the convergence histories between explicit and implicit time-marching is shown in Fig. 3(a). The "error" in the solution was taken to be the $L_2$-norm of the density residual. As shown in Fig. 3(a), the explicit solution is very slow to converge. This solution takes approximately 10,000 time steps to become converged to engineering accuracy, which is taken to be a four order of magnitude reduction in solution error. In contrast, the implicit solution is converged to four orders of magnitude in only approximately 500 steps and is converged to machine zero in less than 2000 steps. The implicit solution costs approximately 75% more per time step than the explicit solution because of the increased number of operations required to evaluate the flux jacobians. This increase in CPU time is far out-weighed by the faster convergence to steady state in that a converged solution is obtained with the implicit relaxation scheme with an order of magnitude less CPU time than the explicit scheme. The resulting steady pressure distribution is shown in Fig. 3(b). For this case there is a relatively strong shock wave on the upper surface of the airfoil near 62% chord and a relatively weak shock wave on the lower surface near 30% chord. The pressure distribution indicates that there is only one grid point within the shock structure, on either the upper or lower surface of the airfoil, due to the sharp shock capturing ability of flux-vector splitting.

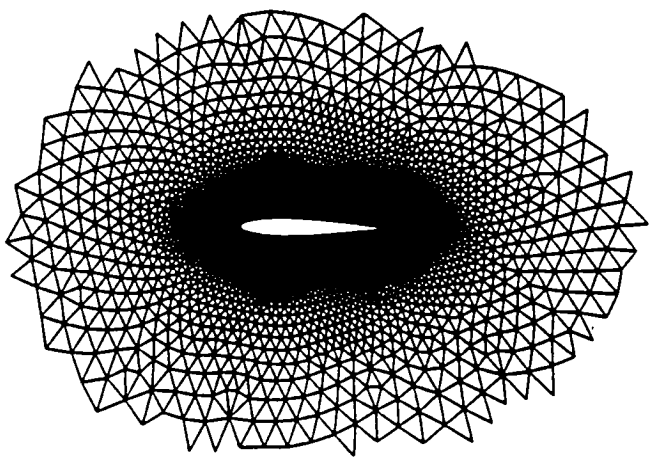

Fig. 2 Partial view of unstructured grid of triangles about the NACA 0012 airfoil.

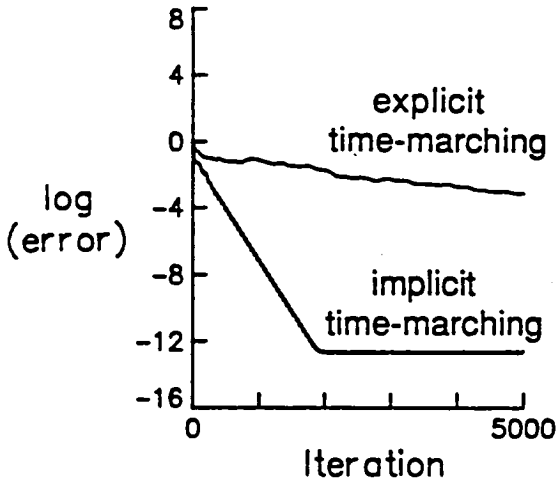


(a) convergence histories.

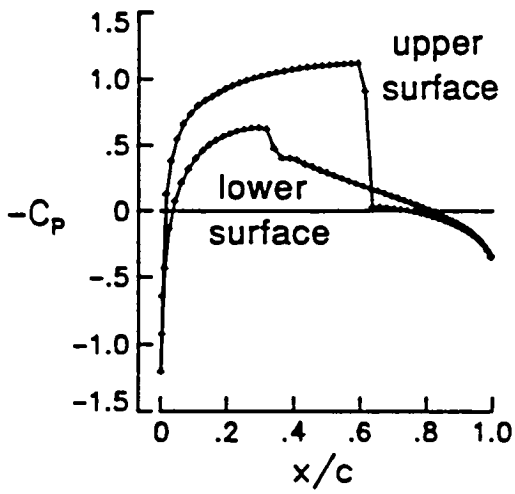


(b) steady pressure distribution.

Fig. 3 Comparison of steady-state results for the NACA 0012 airfoil at $M_\infty = 0.8$ and $\alpha = 1.25°$.

To assess the accuracy of the three-dimensional, unstructured-grid, upwind-Euler algorithm, calculations were performed for the ONERA M6 wing.[19] The M6 wing has a leading edge sweep angle of 30°, an aspect ratio of 3.8, and a taper ratio of 0.562. The airfoil section of the wing is the ONERA "D" airfoil which is a 10% maximum thickness-to-chord ratio conventional section. The results were obtained using a grid which has 154,314 nodes and 869,056 tetrahedra. The surface triangulation for the upper surface of the wing is shown in Fig. 4 and a partial view of the mesh in the symmetry plane is shown in Fig. 5. The mesh in the symmetry plane reveals how coarse the mesh actually is off of the surface of the wing. The results were obtained using the explicit time-marching scheme since it requires half of the memory of the implicit scheme. The code was run for 6000 time steps at a CFL number of 5.0. The solution required approximately 150 hours of CPU time and 125 million words of memory on the Cray-2 computer at the Numerical Aerodynamic Simulation facility located at NASA Ames Research Center.

Figure 6 shows surface pressure coefficient comparisons with the experimental data at five span stations including $\eta$ = 0.2, 0.44, 0.65, 0.9, and 0.95. In these plots the Euler results are given by the solid curves where plus signs have been included to indicate the actual grid point values which are connected with straight line segments. The experimental data is represented by the circles. For $\eta$ = 0.2 shown in Fig. 6(a), there are two shock waves along the chord. The forward shock wave is well predicted including the suction peak. The second shock wave is predicted slightly downstream of the experimental shock location which is typical of inviscid methods for this case. Also, the lower surface pressure coefficients agree well with the data. At $\eta$ = 0.44 shown in Fig. 6 (b), the shock locations have begun to coalesce. The leading edge suction peak is well predicted and both shock waves are captured sharply. At $\eta$ = 0.65 shown in Fig. 6(c), the forward shock wave is near 20% chord and the second shock wave is near midchord. All of the pressure levels are well predicted and both shocks are captured sharply with only one grid point within the shock structure. There are also no overshoots or undershoots near the shocks due to the flux limiting. Furthermore, the lower surface pressure coefficients are predicted accurately. At $\eta$ = 0.9 shown in Fig. 6(d), the two shocks have merged to form a single, relatively strong, shock wave near 25% chord. Here the shock is very sharply captured and the calculated pressures again agree well with the experimental data. Finally at $\eta$ = 0.95 shown in Fig. 6(e), the shock wave is slightly stronger than the previous span station. Here, the calculated shock also has only one interior point. For this case though, the pressure level upstream of the shock is slightly underpredicted due to the coarseness of the mesh.

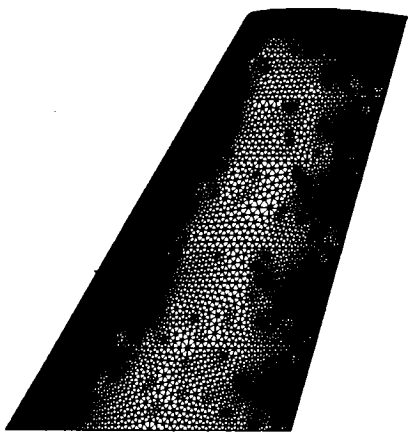

Fig. 4 Upper surface grid for the ONERA M6 wing.

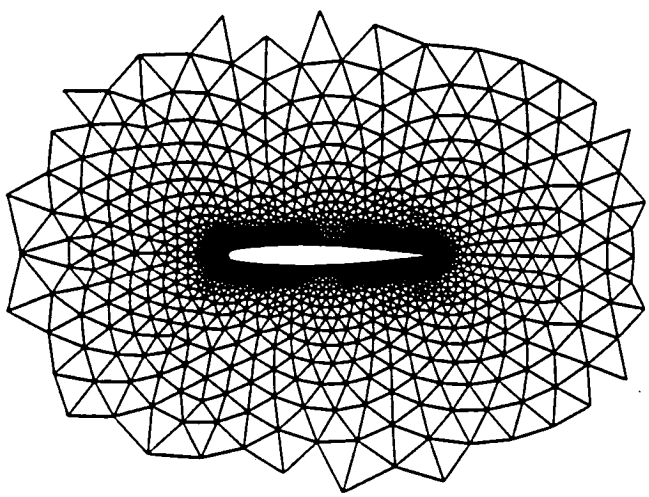

Fig. 5 Partial view of symmetry plane mesh for the ONERA M6 wing.

Figure 7 shows pressure contour lines on the surface of the wing plotted using an increment of $\Delta p$ = 0.02. Pressure contours on the upper surface are shown in Fig. 7(a); Pressure contours on the lower surface are shown in Fig. 7(b). The upper surface contours (Fig. 7(a)) clearly show the lambda-type shock wave pattern formed by the two inboard shock waves which merge together near 80% semispan to form the single strong shock wave in the outboard region of the wing. Also, the forward shock wave appears to be more sharply captured than the second shock wave. This, however, is due to the mesh being more dense in this region than in the midchord region. The lower surface contours (Fig. 7(b)) indicate that there is very little spanwise variation in pressure.

## Concluding Remarks

Improved algorithms for the solution of the three-dimensional time-dependent Euler equations are presented for aerodynamic analysis involving unstructured dynamic meshes. The improvements have been developed recently to the spatial and temporal discretizations used by unstructured grid flow solvers. The improved spatial discretization involves a flux-split approach which is naturally dissipative and captures shock waves sharply with at most one grid point within the shock structure. The temporal discretization involves either an explicit time-integration scheme using a multi-stage Runge-Kutta procedure or an implicit time-integration scheme using a Gauss-Seidel relaxation procedure which is computationally efficient for either steady or unsteady flow problems. With the implicit Gauss-Seidel procedure, very large time steps may be used for rapid convergence to steady state, and the step size for unsteady cases may be selected for temporal accuracy rather than for numerical stability.

Steady flow results are presented for both the NACA 0012 airfoil and the ONERA M6 wing to demonstrate applications of the new Euler solver. The steady results showed that rapid convergence to steady state could be achieved with the implicit time-marching in comparison with results obtained using explicit time-marching. A factor of ten reduction in computational cost was obtained for the case that was presented. Steady flow results were also presented for the ONERA M6 wing to determine the accuracy of the three-dimensional capabilitiy. Only explicit time-marching was used because of the large amount of computer memory that was required. The computed surface pressure coefficients showed

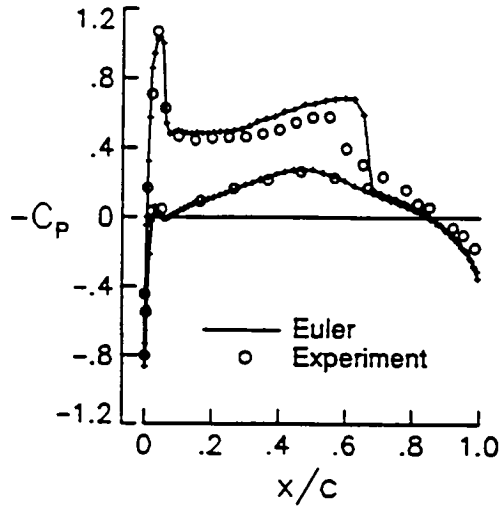


(a) $\eta$ = 0.2.

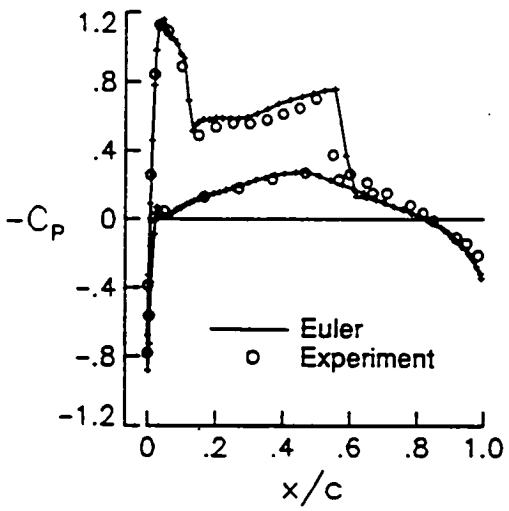


(b) $\eta$ = 0.44.

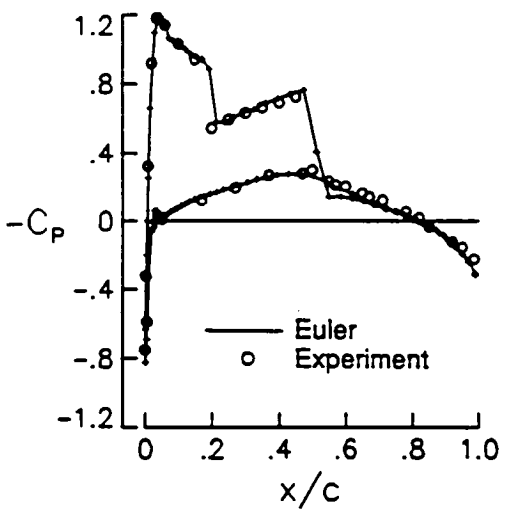


(c) $\eta$ = 0.65.

that the shock waves were captured sharply with only one grid point within the shock structure due to the flux-splitting and there were no overshoots or undershoots near the shocks due to the flux-limiting. The pressure coefficients resembled those that are known to be produced by structured-grid Euler methods and they also agreed well with the experimental data. Future work will focus on validating the implicit time-marching procedures in 3D and extending the methods to solve the Navier-Stokes equations.

## References

[1]Jameson, A.: "Successes and Challenges in Computational Aerodynamics," AIAA Paper No. 87-1184, January 1987.

[2]Edwards, J. W.; and Thomas, J. L.: "Computational Methods for Unsteady Transonic Flows," AIAA Paper No. 87-0107, January 1987. Also chapter 5 in Unsteady Transonic Aerodynamics, ed. by D. Nixon, vol. 120 in AIAA Progress in Astronautics and Aeronautics, September 1989.

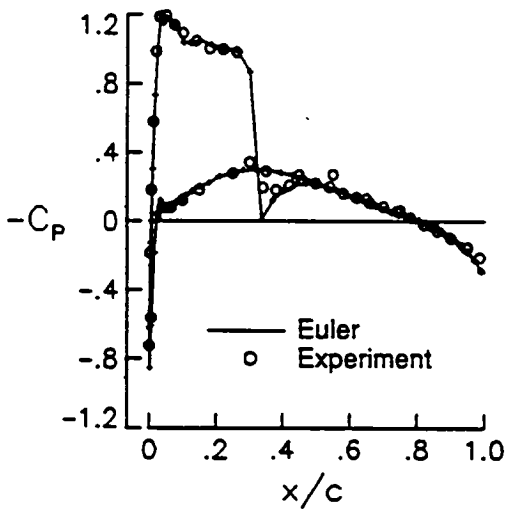


(d) $\eta$ = 0.9.

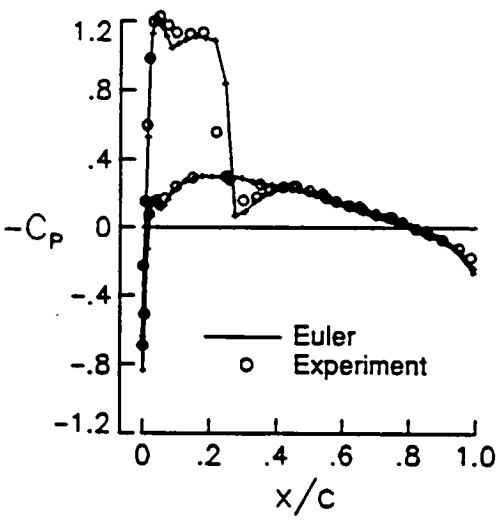


(e) $\eta$ = 0.95.

Fig. 6 Comparisons between calculated and experimental surface pressure coefficients for the ONERA M6 wing at $M_\infty$ = 0.84 and $\alpha$ = 3.06°.

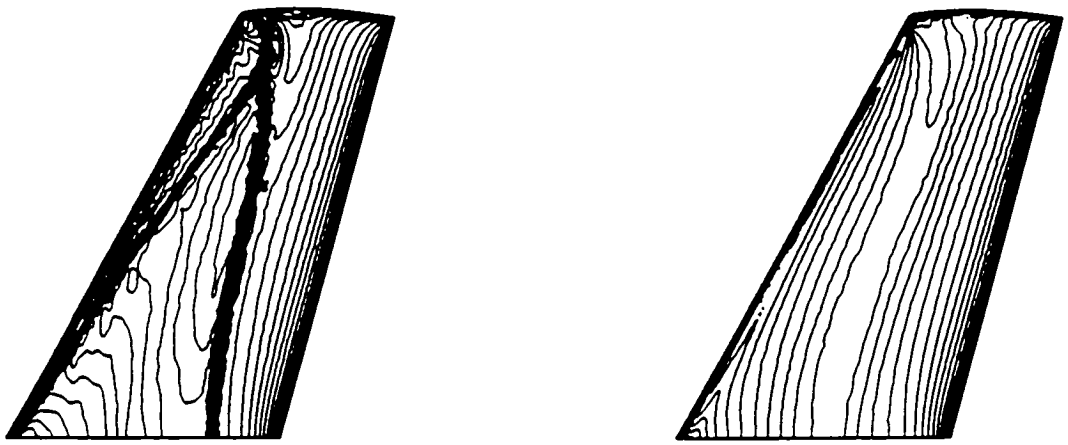

(a) upper surface. (b) lower surface.

Fig. 7 Surface pressure contour lines ($\Delta p = 0.02$) on the ONERA M6 wing at $M_\infty = 0.84$ and $\alpha = 3.06°$.


[3]Jameson, A.; and Mavriplis, D. J.: "Finite Volume Solution of the Two-Dimensional Euler Equations on a Regular Triangular Mesh," AIAA Journal, vol. 24, April 1986, pp. 611-618.

[4]Mavriplis, D. J.: "Multigrid Solution of the Two-Dimensional Euler Equations on Unstructured Triangular Meshes," AIAA Journal, vol. 26, July 1988, pp. 824-831.

[5]Jameson, A.; Baker, T. J.; and Weatherill, N. P.: "Calculation of Inviscid Transonic Flow Over a Complete Aircraft," AIAA Paper No. 86-0103, January 1986.

[6]Morgan, K.; and Peraire, J.: "Finite Element Methods for Compressible Flow," Von Karman Institute for Fluid Dynamics Lecture Series 1987-04, Computational Fluid Dynamics, March 2-6, 1987.

[7]Lohner, R.: "Finite Elements in CFD: What Lies Ahead," International Journal for Numerical Methods in Engineering, vol. 24, 1987, pp. 1741-1756.

[8]Morgan, K.; Peraire, J.; Thareja, R. R.; and Stewart, J. R.: "An Adaptive Finite Element Scheme for the Euler and Navier-Stokes Equations," AIAA Paper No. 87-1172, 1987.

[9]Peraire, J.; Peiro, J.; Formaggia, L.; and Morgan, K.: "Finite Element Euler Computations in Three Dimensions," AIAA Paper No. 88-0032, January 1988.

[10]Batina, J. T.: "Unsteady Euler Airfoil Solutions Using Unstructured Dynamic Meshes," AIAA Paper No. 89-0115, January 1989.

[11]Rausch, R. D.; Batina, J. T.; and Yang, H. T.: "Euler Flutter Analysis of Airfoils Using Unstructured Dynamic Meshes," Journal of Aircraft, vol. 27, May 1990, pp. 436-443.

[12]Batina, J. T.: "Unsteady Euler Algorithm with Unstructured Dynamic Mesh for Complex-Aircraft Aeroelastic Analysis," AIAA Paper No. 89-1189, April 1989.

[13]Barth, T. J.; and Jespersen, D. C.: "The Design and Application of Upwind Schemes on Unstructured Meshes," AIAA Paper No. 89-0366, January 1989.

[14]Whitaker, D. L.; and Grossman, B.: "Two-Dimensional Euler Computations on a Triangular Mesh Using an Upwind, Finite-Volume Scheme, " AIAA Paper No. 89-0470, January 1989.

[15]Batina, J. T.: "Vortex-Dominated Conical-Flow Computations Using Unstructured Adaptively-Refined Meshes," AIAA Paper No. 89-1816, June 1989.

[16]Lee, E. M.; and Batina, J. T.: "Conical Euler Solution for a Highly-Swept Delta Wing Undergoing Wing-Rock Motion," NASA TM 102609, March 1990.

[17]Van Leer, B.: "Flux-Vector Splitting for the Euler Equations," Lecture Notes in Physics, vol. 170, 1982, pp. 507-512.

[18]Batina, J. T.: "Implicit Flux-Split Euler Schemes for Unsteady Aerodynamic Analysis Involving Unstructured Dynamic Meshes," AIAA Paper No. 90-0936, April 1990.

[19]Schmitt, V.; and Charpin, F.: "Pressure Distribution on the ONERA M6 Wing at Transonic Mach Numbers," Appendix B1 in AGARD-AR-138, Experimental Data Base for Computer Program Assessment, May 1979.

NASA National Aeronautics and Space Administration

# Report Documentation Page

| 1. Report No. | 2. Government Accession No. | 3. Recipient's Catalog No. |
|---|---|---|
| NASA TM-102731 | | |

**4. Title and Subtitle**
Three-Dimensional Flux-Split Euler Schemes Involving Unstructured Dynamic Meshes

**5. Report Date**
November 1990

**6. Performing Organization Code**

**7. Author(s)**
John T. Batina

**8. Performing Organization Report No.**

**10. Work Unit No.**
505-63-50-12

**9. Performing Organization Name and Address**
NASA Langley Research Center
Hampton, Virginia 23665-5225

**11. Contract or Grant No.**

**13. Type of Report and Period Covered**
Technical Memorandum

**12. Sponsoring Agency Name and Address**
National Aeronautics and Space Administration
Washington, DC 20546-0001

**14. Sponsoring Agency Code**

**15. Supplementary Notes**
Presented as AIAA Paper No. 90-1649 at the AIAA 21st Fluid Dynamics, Plasma Dynamics and Lasers Conference, Seattle, Washington, June 18-20, 1990.

**16. Abstract**

Improved algorithms for the solution of the three-dimensional time-dependent Euler equations are presented for aerodynamic analysis involving unstructured dynamic meshes. The improvements have been developed recently to the spatial and temporal discretizations used by unstructured grid flow solvers. The spatial discretization involves a flux-split approach which is naturally dissipative and captures shock waves sharply with at most one grid point within the shock structure. The temporal discretization involves either an explicit time-integration scheme using a multi-stage Runge-Kutta procedure or an implicit time-integration scheme using a Gauss-Seidel relaxation procedure which is computationally efficient for either steady or unsteady flow problems. With the implicit Gauss-Seidel procedure, very large time steps may be used for rapid convergence to steady state, and the step size for unsteady cases may be selected for temporal accuracy rather than for numerical stability. Steady flow results are presented for both the NACA 0012 airfoil and the ONERA M6 wing to demonstrate applications of the new Euler solvers. The paper presents a description of the Euler solvers along with results and comparisons which assess the capability.

| 17. Key Words (Suggested by Author(s)) | 18. Distribution Statement |
|---|---|
| Unsteady Aerodynamics<br>Computational Fluid Dynamics<br>Transonic Flow | Unclassified - Unlimited<br>Subject Category 02 |

| 19. Security Classif. (of this report) | 20. Security Classif. (of this page) | 21. No. of pages | 22. Price |
|---|---|---|---|
| Unclassified | Unclassified | 8 | A02 |